

Article

Enhanced Lithium Storage Performance in Si/MXene Porous Composites

Hao Yang, Tingting Jiang *  and Yingke Zhou *

The State Key Laboratory of Refractories and Metallurgy, College of Materials and Metallurgy, Wuhan University of Science and Technology, Wuhan 430081, China; haoyang@wust.edu.cn

* Correspondence: ttjiang@wust.edu.cn (T.J.); zhouyk@wust.edu.cn (Y.Z.)

Abstract: As a potential negative electrode material for lithium-ion batteries (LIBs), silicon has a relatively high specific lithium storage capacity. However, the large volume change during the cycle may result in the isolation with the current collector and therefore the rapid capacity decay during cycling. The poor electric conductivity of the silicon limits the high-power density application in LIBs. To meet the above challenges, a stable Si/Ti₃C₂T_x composite material was designed. Si nanoparticles are bonded with -NH₂ group so that the silicon surface has a positive charge, which can then be electrostatic self-assembly with negatively charged MXene nanosheets in a facile freeze-drying method. Silicon nanoparticles were anchored on the surface or inside the interspace of the MXene nanosheets, which could improve the conductivity of the composites. The composite material (NH₂-Si/MXene) presented a stable and porous structure with extra room for silicon expansion and plentiful channels for carrier transportation. Benefiting from the improved structural stability and enhanced charge storage dynamics, the discharge capacity of NH₂-Si/MXene is 1203.3 mAh g⁻¹ after 100 cycles at 200 mA g⁻¹. These results provide new insights for the application of silicon-based negative electrode materials in high-energy-density LIBs.

Keywords: Li-ion batteries; Ti₃C₂T_x MXene; silicon negative electrode; electrostatic self-assembly



Citation: Yang, H.; Jiang, T.; Zhou, Y. Enhanced Lithium Storage Performance in Si/MXene Porous Composites. *Inorganics* **2023**, *11*, 279. <https://doi.org/10.3390/inorganics11070279>

Academic Editor: Roberto Nisticò

Received: 2 June 2023

Revised: 27 June 2023

Accepted: 28 June 2023

Published: 29 June 2023



Copyright: © 2023 by the authors. Licensee MDPI, Basel, Switzerland. This article is an open access article distributed under the terms and conditions of the Creative Commons Attribution (CC BY) license (<https://creativecommons.org/licenses/by/4.0/>).

1. Introduction

To meet the demand for energy storage devices with higher energy density, the development of lithium-ion battery (LIB) electrode materials has gained much attention. At present, the specific capacity of commercial graphite negative electrode materials is close to the theoretical value (372 mAh g⁻¹), and silicon (Si) has attracted the attention of researchers because of its high theoretical specific capacity [1]. However, during the lithiation/delithiation process, the large expansion of the silicon may cause severe mechanical stress, leading to the pulverization of the silicon and further the continuous worsening of the cycling capacity [2,3]. In addition, due to the crack of silicon, an unstable solid electrolyte interface (SEI) is prone to form consistently and therefore the extra and irreversible consumption of Li-ion in electrolytes [4,5].

Several solutions have been proposed to address these challenges, such as reducing the size of Si to the nanoscale [6,7], coating Si with a protective layer [8,9], and constructing silicon/carbon composites [10,11]. The dispersion of silicon into the carbon material can buffer the volume change of silicon during charging/discharging and to improve electrical conductivity simultaneously is demonstrated to be effective due to the moderate mechanical property and excellent electrical conductivity of carbon. To improve the capacity retention performance of silicon-based materials, various carbon materials were used as buffer layers, including graphene [12,13], graphite [14], carbon nanofibers [15,16], carbon nanotubes [17,18] and mesoporous carbon [19]. Recently, MXene, a new type of two-dimensional transition metal carbide or carbonitride, has attracted wide attention in energy storage applications because of its special structure and chemical properties.

MXene, whose molecular formula is $M_{n+1}X_nT_x$, has good conductivity, electrochemical performance and structural stability. $Ti_3C_2T_x$, as the most representative material in the MXene family, has been widely used in supercapacitors [20], electrochemical sensors [21], and LIBs [22]. Benefiting from the structural and functional advantages, MXene can act as a buffer matrix for silicon-based electrode materials in LIBs [23,24]. Jiang et al. [25] prepared a Si/MXene@CNFs composite material by a simple electrospinning method. Zhang et al. [26] prepared sandwich-like silicon/ $Ti_3C_2T_x$ composites with silicon nanoparticles (SiNPs) and multi-layered $Ti_3C_2T_x$ nanosheets by electrostatic self-assembly. After 100 cycles at the specific current of 300 mA g^{-1} , the composite showed an excellent capacity of 643.8 mAh g^{-1} . MXene nanosheets have also been used as a matrix to hold silicon and other 1-dimensional materials to achieve better charge transfer. For instance, the Si/MXene@CNFs composite still maintained the excellent capacity of 440.3 mAh g^{-1} after 200 cycles at the specific current of 1 A g^{-1} . Although the electrochemical performance of Si could be improved by the combination with MXene, the exposed SiNPs on the surface of MXene are prone to easily crush or exfoliate during the cycling due to the difference in volume expansion rates and the weak force between the two materials [27,28].

Herein, a three-dimensional porous composite material is prepared by a simple electrostatic self-assembly method. NH_2 -Si/MXene composites were formed by electrostatic self-assembly of MXene nanosheets prepared by chemical etching and aminated SiNPs. NH_2 -Si/MXene composite as a LIB negative electrode has the following advantages: SiNPs are dispersed in the structural frame formed by MXene nanosheets. SiNPs with amino-group on the surface could maintain the strong electrostatic interaction with MXene nanosheets to prevent exfoliation and lose connection with the current collector, while MXene nanosheets could act as a matrix and provide extra space for volume change of silicon. According to the mass ratio of NH_2 -Si to MXene (1:1, 3:1 and 5:1), they are labeled as NH_2 -Si1/MXene1, NH_2 -Si3/MXene1 and NH_2 -Si5/MXene1, respectively. The rational-designed composites could deliver a high specific discharge capacity of $1203.3 \text{ mAh g}^{-1}$ after 100 cycles at 200 mA g^{-1} . The impact of the mass ratio of MXene in the composites has also been compared, and the active material containing 25 wt.% exhibits the most stable cyclic capacity.

2. Materials and Methods

2.1. Preparation of $Ti_3C_2T_x$ MXene

1.6 g LiF was added to 20 mL HCl (12 M) solution and agitated for 10 min at $30 \text{ }^\circ\text{C}$ in a Teflon container. Thereafter, 1 g Ti_3AlCl_2 (MAX, 400 mesh) was slowly added to the above mixture and kept at $30 \text{ }^\circ\text{C}$ under magnetic stirring for 24 h. After etching, the precipitate was washed with deionized water, and black slurry-like precipitation was collected by centrifugation (3500 rpm) until the solution is neutral. The precipitation was then ultrasonic for 2 h with an inert gas argon atmosphere. Finally, the supernatant was collected after centrifugation at 3500 rpm for 1 h to obtain MXene solution. MXene colloidal solution consists of both multilayer and few-layer $Ti_3C_2T_x$ nanosheets.

2.2. Fabrication of NH_2 -Si/MXene Composite

An amount of 100 mg of silicon nanoparticles (~100 nm, Shanghai Naiou Nano Technology Co., Shanghai, China) were ultrasonically dispersed in 60 mL ethanol for 1 h, and then 1 mL of (3-aminopropyl) triethoxysilane (APTES) was added and stirred magnetically for 6 h at $30 \text{ }^\circ\text{C}$ to obtain SiNPs decorated with an amino group (NH_2 -Si). NH_2 -Si was then washed in ethanol to remove the excess APTES and dried overnight. The collected NH_2 -Si was added to the prepared MXene aqueous solution slowly. After stirring for 1 h, the mixed solution of NH_2 -Si and MXene was freeze-dried to obtain the columnar porous structure (NH_2 -Si/MXene). According to the mass ratio of NH_2 -Si to MXene (1:1, 3:1 and 5:1), they were labeled as NH_2 -Si1/MXene1, NH_2 -Si3/MXene1 and NH_2 -Si5/MXene1, respectively.

2.3. Material Characterization

The micromorphology of NH₂-Si/MXene was observed by scanning electron microscope (SEM) (PHILIPS XL30TMP). The element distribution of the sample was analyzed by means of energy dispersion X-ray spectrometer (EDS, OXFORD IET200). X-ray powder diffraction (XRD) patterns with a scanning range of 5–90° were obtained using Xpert Pro MPD. The transmission electron microscopy (TEM) tests were executed on FEI Tecnai G20. X-ray photoelectron spectroscopy (XPS) was performed on AXIS SUPRA+. The specific surface area and pore size were analyzed by Brunner–Emmet–Teller (BET) measurement, which was performed using the Micromeritics ASAP 2460 test instrument from Mack Instruments. N₂ was adsorbed by the static volumetric method.

2.4. Electrochemical Measurement

The above synthesized NH₂-Si/MXene composites were mixed with carboxymethyl cellulose (CMC) binders and Super P carbon at a weight ratio of 7:1.5:1.5 in deionized water and stirred for 8 h to form a uniform slurry. After coating the slurry of active materials, the copper foil was then dried under 80 °C in vacuum for 16 h. For comparison, pure silicon was used as a reference sample to prepare electrodes in the same process. To investigate the electrochemical performance, the CR2032 coin cells were assembled in a glove box filled with argon gas. Li foil was used as the counter electrode and reference electrode, while the copper foil with active material served as the working electrode. The separator was Celgard 2500 polypropylene. The electrolyte used was 1 M LiPF₆, the volume ratio of 1:1 diethyl carbonate (DEC) and ethylene carbonate (EC), and 5% fluoroethylene carbonate (FEC) and 1% vinyl carbonate (VC) was added.

Cyclic voltammetry (CV) and electrochemical impedance spectroscopy (EIS) investigations were performed on the Bio-Logic VMP3. The CV test voltage range was 0.01–1.5 V, and the frequency range in EIS was 10 mHz–100 kHz. Galvanostatic charging and discharging were performed by the NEWARE BTS (5 V, 50 mA) test system with a voltage range of 0.01–1.5 V.

3. Results and Discussion

3.1. Material Characterization

The synthetic process of the NH₂-Si/MXene composites is shown in Figure 1. A large number of groups such as -F, -OH, -O and -Cl exist on the surface of Ti₃C₂T_x MXene prepared by the etching process [29]. The presence of these groups makes MXene negatively charged and uniformly dispersed in water [30]. After modification by (3-aminopropyl) triethoxysilane (APTES), the surface of SiNPs is decorated with a positively charged -NH₂ group [31]. Positively charged SiNPs decorated with an amino group (NH₂-Si) nanoparticles and negatively charged MXene could be tightly linked due to electrostatic attraction. The stable porous structure of NH₂-Si and MXene composites was then obtained by freeze-drying.

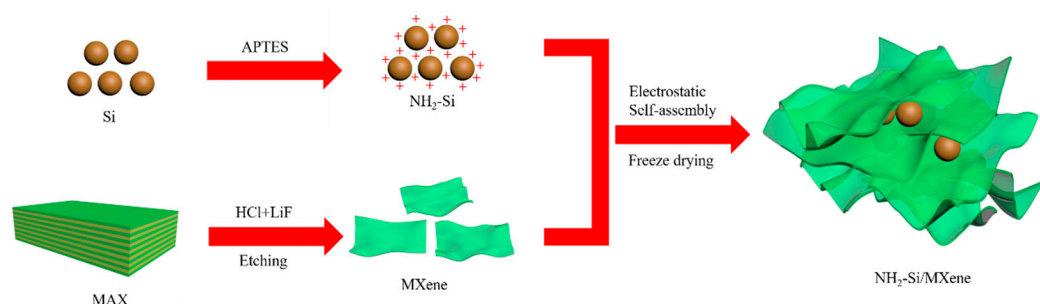


Figure 1. Schematic diagram of the synthesis process of NH₂-Si/MXene composites.

Figure 2a shows the XRD patterns of the MAX, MXene, and NH₂-Si₃/MXene1, respectively. After etching away the Al layers from Ti₃AlC₂, the (002) peak was shifted from 9.62°

to a smaller angle of 5.85° , indicating the successful synthesis of $\text{Ti}_3\text{C}_2\text{T}_x$ nanosheets [32]. After compositing with silicon, the diffraction peaks locate at 28.28° , 47.16° , 55.98° , 69.15° , 76.24° , and 87.87° , respectively, corresponding to the (111), (220), (311), (400), (331), and (422) planes of the Si (JCPDS No. 27-1402) [33]. The peak at 25.11° belongs to the (101) plane of TiO_2 [34]. This is due to the partial oxidation reaction on the surface of MXene during the composite processing. During synthesis, no other phases can be observed in the prepared $\text{NH}_2\text{-Si3/MXene1}$ composite. Composites with different Si weight ratios ($\text{NH}_2\text{-Si1/MXene}$ and $\text{NH}_2\text{-Si5/MXene1}$) exhibit similar XRD patterns, except for various strength of MXene and TiO_2 characteristic peaks.

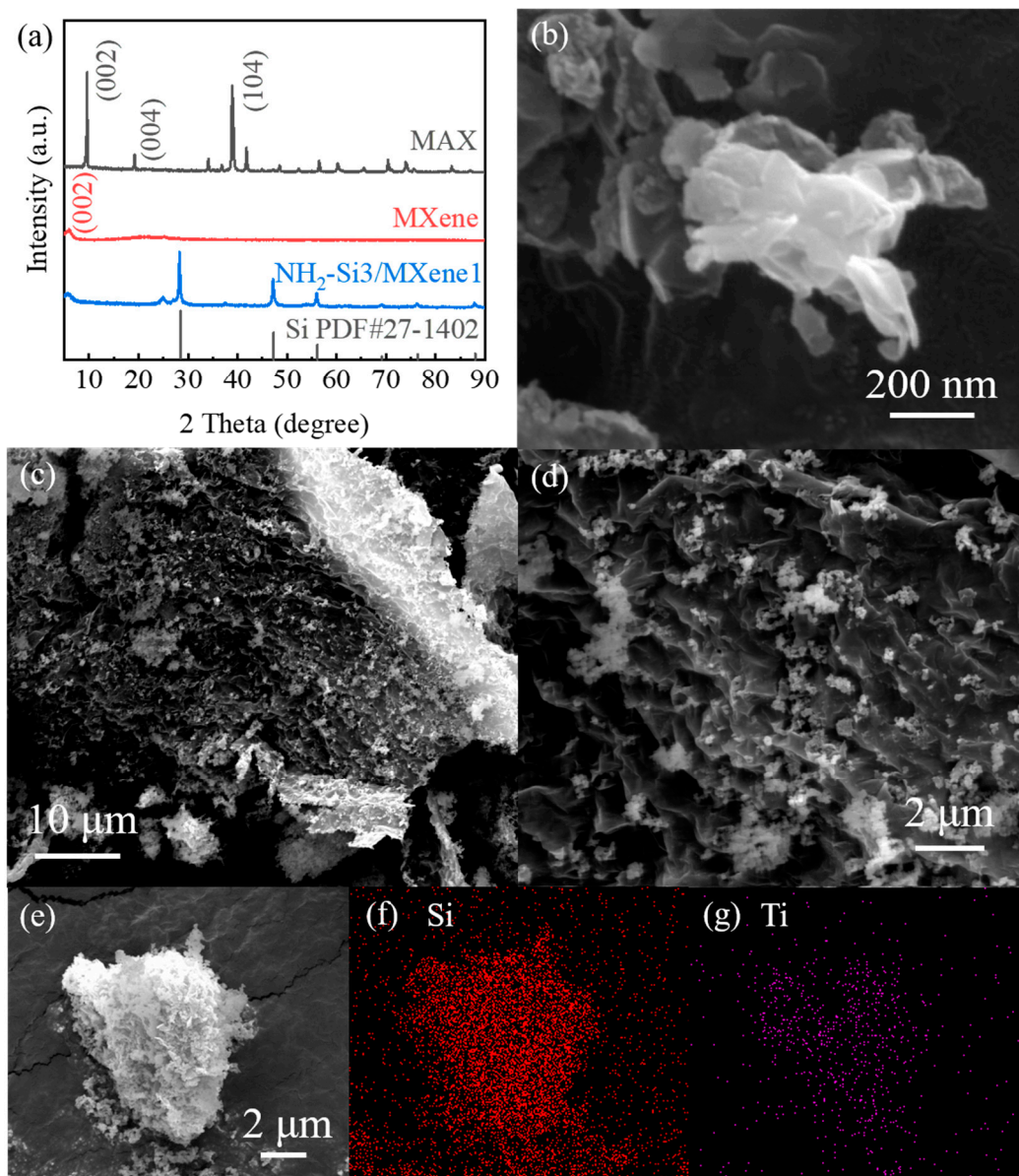


Figure 2. (a) The XRD patterns of MAX, MXene, and $\text{NH}_2\text{-Si3/MXene1}$. (b) SEM image of MXene. (c–e) SEM and (f,g) SEM–EDS elemental mapping of $\text{NH}_2\text{-Si3/MXene1}$ composites.

The microstructure in the composite was characterized by SEM. As shown in Figure 2b, the $\text{Ti}_3\text{C}_2\text{T}_x$ MXene was etched into nanosheets with few layers. The morphology of the $\text{NH}_2\text{-Si3/MXene1}$ composites is shown in Figure 2c,d. MXene nanosheets stack and interact with each other to form a porous network. $\text{NH}_2\text{-Si}$ nanoparticles are evenly dispersed between the MXene to form a stable three-dimensional structure. The positively charged SiNPs modified by APTES could attract the negatively charged $\text{Ti}_3\text{C}_2\text{T}_x$ MXene nanosheets

through electrostatic interaction and prevent aggregation and stacking of nanosheets. Similar porous morphologies of $\text{NH}_2\text{-Si1/MXene1}$ and $\text{NH}_2\text{-Si5/MXene1}$ are shown in Figure S2. Due to the large amount of MXene in $\text{NH}_2\text{-Si1/MXene1}$, it can be seen that the $\text{NH}_2\text{-SiNPs}$ are dispersed in the MXene layers, while MXene nanosheets are aggregated and stacked. In $\text{NH}_2\text{-Si5/MXene1}$ composites, a large number of SiNPs are agglomerated and attached to the surface of MXene nanosheets. Therefore, $\text{NH}_2\text{-Si3/MXene1}$ presents the most uniform distribution of SiNPs and MXene nanosheets, and the moderate porous structure. As evidenced by EDS mappings (Figure 2f,g), Si and Ti elements are evenly distributed in the $\text{NH}_2\text{-Si3/MXene1}$ composites, indicating the uniform distribution of SiNPs in the MXene matrix. The aggregation of SiNPs or MXene nanosheets may result in structure collapse and hinder the carrier transportation in the active materials.

TEM characterization of the $\text{NH}_2\text{-Si3/MXene1}$ composites was further performed to reveal the morphology and connection of the MXene and SiNPs (Figure 3). As shown in Figure 3a,b, SiNPs with a diameter of 100 nm are anchored and coated on MXene in the middle of the composite, and MXene sheets are wrapped around the Si particles, where the tight binding of SiNPs to MXene can be clearly observed. There is a large amount of void in the composite which could provide extra room for the volume expansion of Si. The lattice fringe of SiNPs and MXene can be analyzed by high-resolution TEM (HRTEM) (Figure 3c). The interplanar spacing of 0.32 nm and 1.1 nm correspond to Si (111) plane and $\text{Ti}_3\text{C}_2\text{T}_x$ (002) plane, respectively [35]. The pores of $\text{NH}_2\text{-Si3/MXene1}$ composites provide sufficient space for SiNPs expansion, ensuring cycle stability. The porous network in the material can also improve the electrolyte infiltration and promote the transportation of lithium ions. In addition, the conductive network of MXene also facilitates electron migration during lithiation/delithiation.

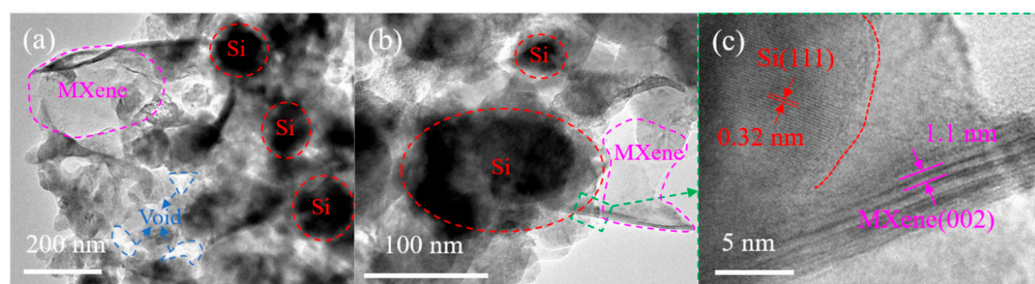


Figure 3. (a,b) TEM images and (c) HRTEM image of $\text{NH}_2\text{-Si3/MXene1}$ composites.

In order to obtain the specific surface area and pore size distribution of the composites, BET measurements on $\text{NH}_2\text{-Si1@MXene1}$, $\text{NH}_2\text{-Si3@MXene1}$, and $\text{NH}_2\text{-Si5@MXene1}$ were carried out and the results were analyzed. The N_2 adsorption isotherms of the studied materials were presented in Figure 4a–c, and the Figure 4d shows the distribution of the pore size of the materials. The desorption curves all belong to type III curves, indicating existence of stacking pores between flakes [36]. The specific surface area values of $\text{NH}_2\text{-Si1@MXene1}$, $\text{NH}_2\text{-Si3@MXene1}$, and $\text{NH}_2\text{-Si5@MXene1}$ are 28.5, 25.7, and 20.3 $\text{m}^2 \text{g}^{-1}$, respectively (See in Table 1). The pores in the composite mainly exist as mesoporous pores (2–50 nm). The specific surface area of the composite decreases with the decrease in MXene content. When MXene is combined with SiNPs, more pores are formed at the composite interface in the materials with higher MXene content, indicating that the pores were mainly from the interstice formed by the combination of MXene and silicon nanoparticles. The pore content further affects the electrochemical properties of the material. The presence of pores in the composite material increases the contact area between the active material and the electrolyte, enhances the permeability of the electrolyte, and reduces the diffusion distance of lithium ions in the composite material, which are conducive to achieving higher lithium-ion storage performance.

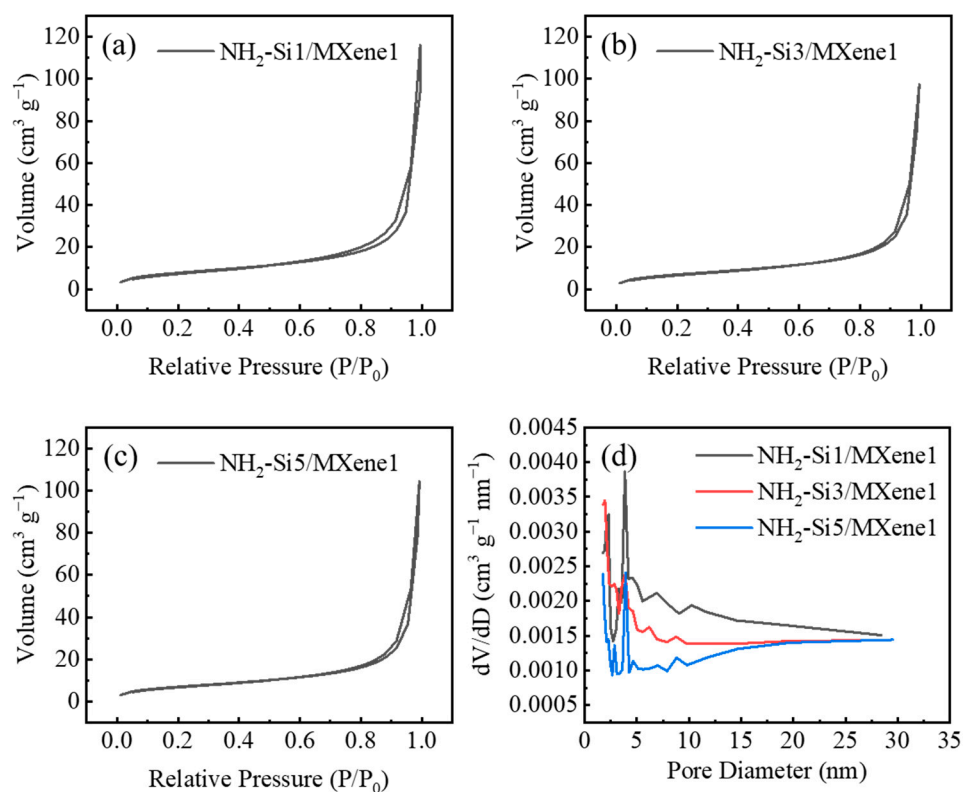


Figure 4. (a–c) Nitrogen desorption curve and (d) pore size distribution of the $\text{NH}_2\text{-Si1/MXene1}$, $\text{NH}_2\text{-Si3/MXene1}$, $\text{NH}_2\text{-Si5/MXene1}$.

Table 1. The specific surface area values of $\text{NH}_2\text{-Si1/MXene1}$, $\text{NH}_2\text{-Si3/MXene1}$ and $\text{NH}_2\text{-Si5/MXene1}$.

Materials	Specific Surface Area ($\text{m}^2 \text{g}^{-1}$)
$\text{NH}_2\text{-Si1/MXene1}$	28.5
$\text{NH}_2\text{-Si3/MXene1}$	25.7
$\text{NH}_2\text{-Si5/MXene1}$	20.3

The bonding structure of $\text{NH}_2\text{-Si3/MXene1}$ composites was investigated by XPS, as shown in Figure 5a–f. The C 1s XPS spectrum (Figure 5b) can be fitted into four separate peaks located at 281.3, 284.8, 286.5, and 288.9 eV, which correspond to the C-Ti, C-Si, C-O, and C=O bonds in the $\text{NH}_2\text{-Si3/MXene1}$ composite, respectively [37]. In the O 1s XPS spectrum (Figure 5c), the binding energies of 529.8, 530.4, 531.9, 532.6, and 533.3 eV are attributed to Ti-O-Ti, C-Ti-OH, Si-OH, C-Ti-O, and Si-O-Si bonds, respectively [24]. The existence of some Ti-O bonds can be ascribed to the oxidation of $\text{Ti}_3\text{C}_2\text{T}_x$ MXene to TiO_2 . In the Si 2p XPS spectrum of the $\text{NH}_2\text{-Si3/MXene1}$ (Figure 5d), the binding energies of Si 2p_{1/2} and Si 2p_{3/2} locate at 98.9 and 99.5 eV, and the binding energies of Si-O are located at 102.6 and 103.3 eV, respectively [38]. In the Ti 2p XPS spectrum (Figure 5e), the peak of 461.1 eV corresponds to the Ti-N peak [39], which is in accordance with the XPS spectrum of N 1s, indicating the successful bonding of $-\text{NH}_2$ group decorated SiNPs with $\text{Ti}_3\text{C}_2\text{T}_x$ MXene through electrostatic attraction.

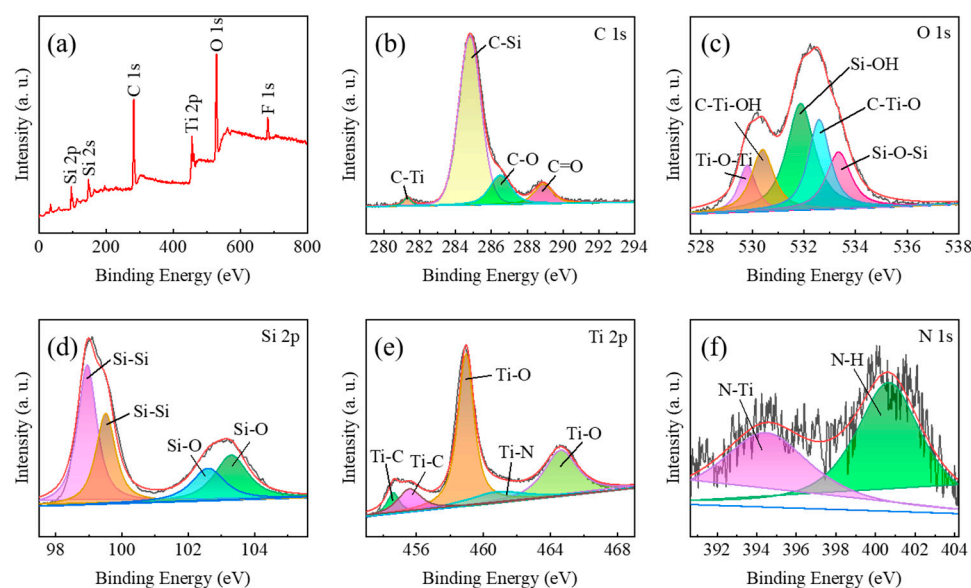
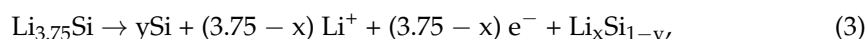
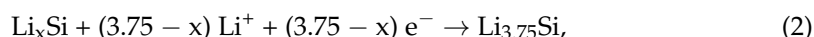


Figure 5. (a) XPS spectra of $\text{NH}_2\text{-Si}_3/\text{MXene}1$, and the corresponding high-resolution XPS spectra of C 1s (b), O 1s (c), Si 2p (d), Ti 2p (e), and N 1s (f).

3.2. Electrochemical Characterization

The electrochemical properties of the samples as negative electrode materials in LIBs were evaluated in half-cells. The electrochemical properties of $\text{NH}_2\text{-Si}_1/\text{MXene}1$, $\text{NH}_2\text{-Si}_3/\text{MXene}1$, $\text{NH}_2\text{-Si}_5/\text{MXene}1$, MXene, and pure Si were investigated. Figure 6a shows the CV test of the $\text{NH}_2\text{-Si}_3/\text{MXene}1$ composite in the potential interval of 0.01 to 1.5 V (vs. Li^+/Li). Since silicon provides most of the capacity in the composite, the potential range between 0.01 V to 1.5 V of the lithiation/delithiation reactions of silicon is chosen as the main testing range. In the CV testing process, the starting potential in the first cycle and the end potential in the third scan are selected according to the open circuit voltage of the half-cell, at about 2.75 V. In the first cathodic scan, a wide reduction peak at around 1.1 to 1.6 V appears, indicating the formation of the SEI layer. The peak at 0.18 V in the subsequent cathodic scan corresponds to the lithiation process from Si to $\text{Li}_{15}\text{Si}_4$, which can be explained by Equations (1) and (2). In the lithiation process of silicon, the alloy reaction occurs gradually, and the peaks of the two reactions are relatively close on the CVs to form a wide peak [40]. The peaks at 0.38 V and 0.56 V in the anodic scan can be attributed to the delithiation process from $\text{Li}_{15}\text{Si}_4$ back to amorphous Si, which corresponds to Equation (3) [41,42].



In addition, the intensity of the peak gradually increases with the cycle, suggesting the activation process of Si/MXene composite. CVs of other samples are shown in Figure S3, exhibiting a similar shape due to the main lithiation and delithiation reaction of Si. Specially, two redox couples at 1.01 V/1.15 V and 2.36 V/2.14 V in the MXene electrode are observed, which belong to the lithium storage process of MXene [43]. The redox peaks at 1.91 V/1.66 V can be ascribed to the charging/discharging process of anatase TiO_2 . Comparing the CVs of composites, MXene and silicon, the peak intensity corresponding to MXene decreases with the increase in the mass ratio of Si.

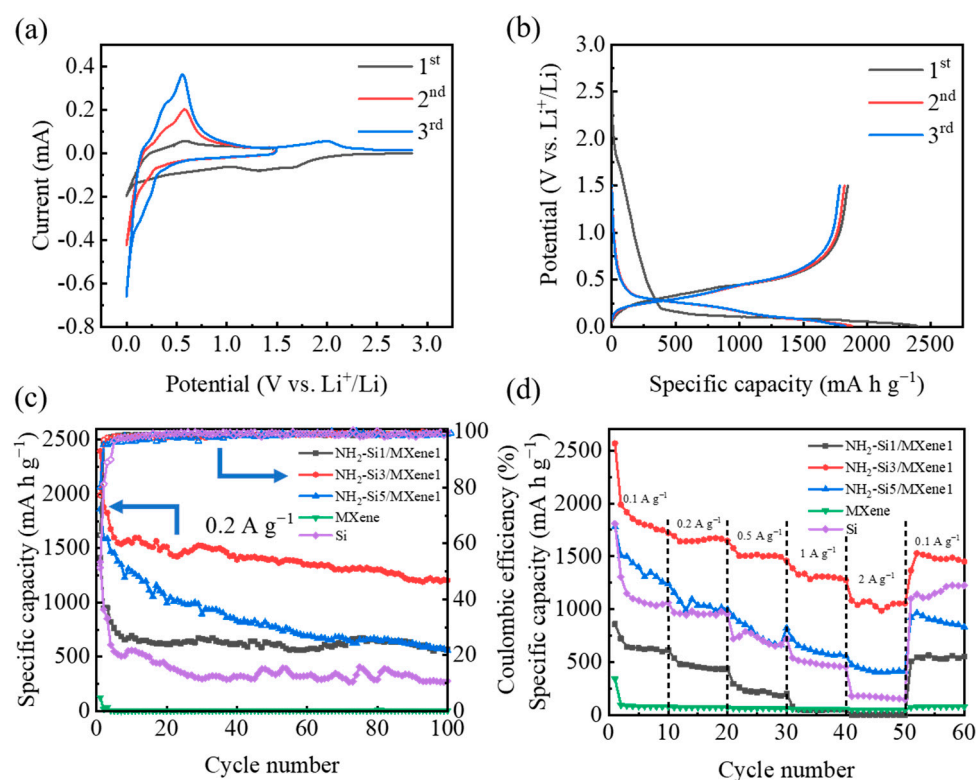


Figure 6. (a) CVs of the first three cycles for $\text{NH}_2\text{-Si3/MXene1}$ at 0.2 mV s^{-1} from 0.01 to 1.5 V. (b) Galvanostatic charge/discharge curves of $\text{NH}_2\text{-Si3/MXene1}$ negative electrodes at 200 mA g^{-1} from 1st to 3rd cycles. (c) Cycling stability of $\text{NH}_2\text{-Si1/MXene1}$, $\text{NH}_2\text{-Si3/MXene1}$, $\text{NH}_2\text{-Si5/MXene1}$, MXene, and Si negative electrodes at 200 mA g^{-1} . (d) Rate capacity of $\text{NH}_2\text{-Si1/MXene1}$, $\text{NH}_2\text{-Si3/MXene1}$, $\text{NH}_2\text{-Si5/MXene1}$, MXene, and Si negative electrodes at various specific currents.

Figure 6b shows the galvanostatic charge/discharge curve of an $\text{NH}_2\text{-Si3/MXene1}$ composite in the first three cycles at the specific current of 0.2 A g^{-1} in a potential range of 0.01 to 1.5 V (vs. Li^+/Li). In the galvanostatic charging/discharging process, the starting discharging potential was set as the open circuit voltage at 2.6 V of the half-cell, and in the subsequent charging and discharging cycles, the potential range was set between 0.01 V and 1.5 V. During the first discharge process, there is a voltage platform at about 0.2 V, corresponding to the lithiation of crystalline silicon and forming an amorphous lithium silicon phase. The slope platforms occur during the charging process below 0.6 V, which is due to the delithiation process. In the first cycle, discharging and charging capacities of $\text{NH}_2\text{-Si3/MXene1}$ are 2395.1 and 1848.4 mAh g^{-1} , respectively, with an initial coulomb efficiency (ICE) of 77.17%, which is much higher than that of pure Si sample. The large initial irreversible capacity loss is mainly attributed to the irreversible formation of the SEI layer on the surface of the active material during the first discharge. The good capacity retention rate indicates the stable structure of the composite and the synergistic effect of silicon and MXene. MXene can act as the matrix of the structure and stay integrated where $\text{NH}_2\text{-SiNPs}$ are strongly wrapped in this porous matrix. The flexibility and strength of MXene could buffer the volume change of silicon in charging/discharging. The better electrochemical properties of $\text{NH}_2\text{-Si3/MXene1}$ composites are attributed to the relatively stable structure due to the suitable mass ratio between MXene and SiNPs, which could slow down the capacity decay rate of the composite. The high mass ratio of Si may lead to the agglomeration of SiNPs, resulting in an unstable structure of $\text{NH}_2\text{-Si/MXene}$ composite. On the other hand, MXene with a large ratio in the composite may reduce the whole specific capacity and the restacking MXene also may lead to the ununiform distribution of Si on MXene. Therefore, the proper mass ratio of Si and MXene can form a uniform and stable composite structure and thus better performance.

To demonstrate the cycling properties of the NH₂-Si/MXene composites, MXene, and silicon, galvanostatic charging and discharging were performed at a specific current of 0.2 A g⁻¹ for 100 cycles, as shown in Figure 6c. All four electrodes that contained silicon exhibit high initial discharging capacity due to the high theoretical specific capacity of silicon. However, the rate of capacity fading varies for different samples. After 100 cycles, the Si/MXene composites all present better capacity stability than pure silicon, indicating the good synergistic effect between the two materials. Among them, the reversible discharging capacity of NH₂-Si3/MXene1 can be maintained at 1203.3 mAh g⁻¹, which is the highest capacity, much higher than that of pure silicon (273.5 mAh g⁻¹). The pure MXene electrode demonstrates low capacity both at the first and after 100 cycles. The NH₂-Si3/MXene1 presents better cycling performance than other previous works, as summarized in Table 2. The good cyclic stability can be attributed to the porous structure of NH₂-Si3/MXene1 composites with plentiful pores and uniformly distributed SiNPs in the MXene matrix via strong bonds, which effectively releases volume variations and maintains the integrity of silicon, thereby improving capacity retention. In addition to good cycle stability, NH₂-Si3/MXene1 composite also exhibits better rate properties. As shown in Figure 6d, the average reversible discharge capacity of the NH₂-Si3/MXene1 composites is 1821.8, 1657.6, 1507.3, 1312.8, and 1046.1 mAh g⁻¹ when the specific currents are 0.1, 0.2, 0.2, 0.5, 1 and 2 A g⁻¹, respectively, indicating better lithiation and delithiation kinetics than other composites and pure silicon. When the specific current returns to 0.1 A g⁻¹, the discharge capacity increases to 1474.8 mAh g⁻¹, which suggests that the NH₂-Si3/MXene1 composite has good reversibility.

Table 2. The comparison of LIBs' negative electrode performances between this work and the similar composites.

Materials	Specific Current (A g ⁻¹)	Initial Capacity (mAh g ⁻¹)	Cycle Number	Reversible Capacity (mAh g ⁻¹)	Ref.
Si@Ti ₃ C ₂ MXene	0.2	1195	150	188	[32]
MXene and Si	0.1	731	500	557.6	[44]
NH ₂ -Si/Ti ₃ C ₂ T _x	0.3	1624.1	100	643.8	[26]
SiO/wrinkled MXene	0.5	1945	100	850	[45]
Si@MXene	0.2	1450	100	981	[46]
Si@Ti ₃ C ₂ T _x	0.5	4392	200	1000	[47]
Si@MXene	0.5	1238.5	150	1003.6	[48]
SiO _x @NTS	0.5	1882.1	100	1141.3	[49]
pSi/MXene	0.1	2843.5	200	1039.3	[50]
NH ₂ -Si/MXene	0.2	2395.1	100	1203.3	This work

To further analyze the electrochemical properties of Si/MXene composites, EIS of NH₂-Si3/MXene1 composite and pure Si are compared as shown in Figure 7a,b. At high frequencies, the diameter of the semicircle refers to the charge transfer resistance (R_{ct}) at the interface between the electrodes and the electrolyte [51]. The R_{ct} attracted from the high-frequency semicircle of the NH₂-Si3/MXene1 composite is 242.6 Ω and 129.1 Ω before and after 100 cycles, respectively, smaller than those of (243.5 Ω and 634.3 Ω). It shows that the compositing of MXene with NH₂-Si into a 3D porous structure can improve the overall conductivity of the electrode and highlight its advantages in electrolyte permeation on the electrode surface. Figure 7c,d show the relationship between the impedance and the phase angle before and after cycles. After 100 cycles, the slope of NH₂-Si3/MXene1 is smaller than Si, indicating a smaller Warburg factor (σ) and a larger Li⁺ ion diffusion coefficient in NH₂-Si3/MXene1. This may come from the lamellar porous structure of NH₂-Si3/MXene1, where the transport length of Li⁺ ions is shorter and the Li⁺ diffusion and migration ability is better. Therefore, the NH₂-Si3/MXene1 composite demonstrates better electrochemical

properties as negative electrode material in LIBs with good cyclic stability, effective charge transportation, and high reversibility.

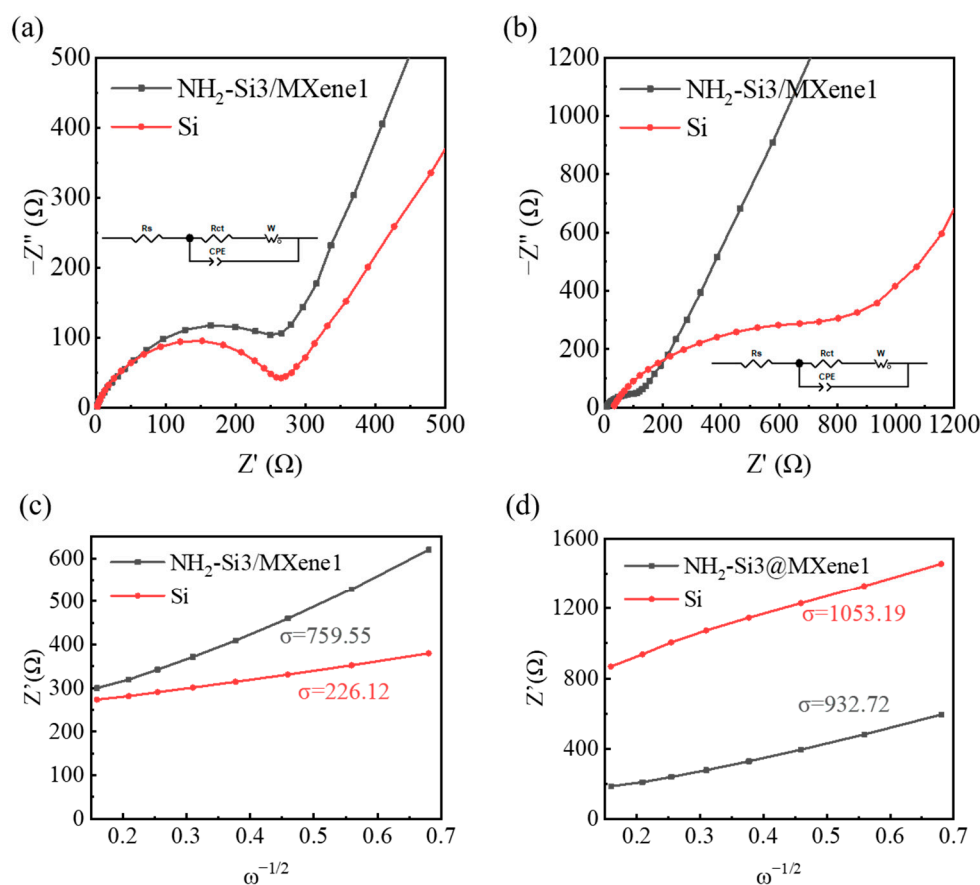


Figure 7. Nyquist plots of the NH₂-Si₃/MXene1 and Si electrodes before (a) and after 100 cycles (b). Relationship between Z' and ω^{1/2} in the low-frequency region before (c) and after 100 cycles (d).

To further study the structural stability of the prepared electrodes, SEM was performed to observe the surface and cross-section micromorphology of NH₂-Si₃/MXene1 and Si electrodes before and after 100 cycles (Figure 8). After 100 cycles, the surface of NH₂-Si₃/MXene1 electrode exhibits smooth and united structure with no cracks existing, suggesting good structural stability. However, there are obvious cracks on the surface of Si electrodes, which is in accordance with the sharp drop in discharge capacity during the cycling. The improvement of the structural stability of NH₂-Si₃/MXene1 is mainly caused by the strong bonds between Si and MXene as well as the integrity of the porous structure of the composite. In the cross-section view in Figure 8e–h, the thicknesses of NH₂-Si₃/MXene1 and Si electrodes before and after cycling can be found. The thickness change of NH₂-Si₃/MXene1 and Si electrodes are 19.7% and 48.8%, respectively, indicating the huge difference in volume expansion ratios of these two electrodes. The low volume expansion ratio of NH₂-Si₃/MXene1 illustrates that the chemical bond formed between NH₂-Si and MXene and the integrated porous structure of the composite plays an important role in forming a stable electrode.

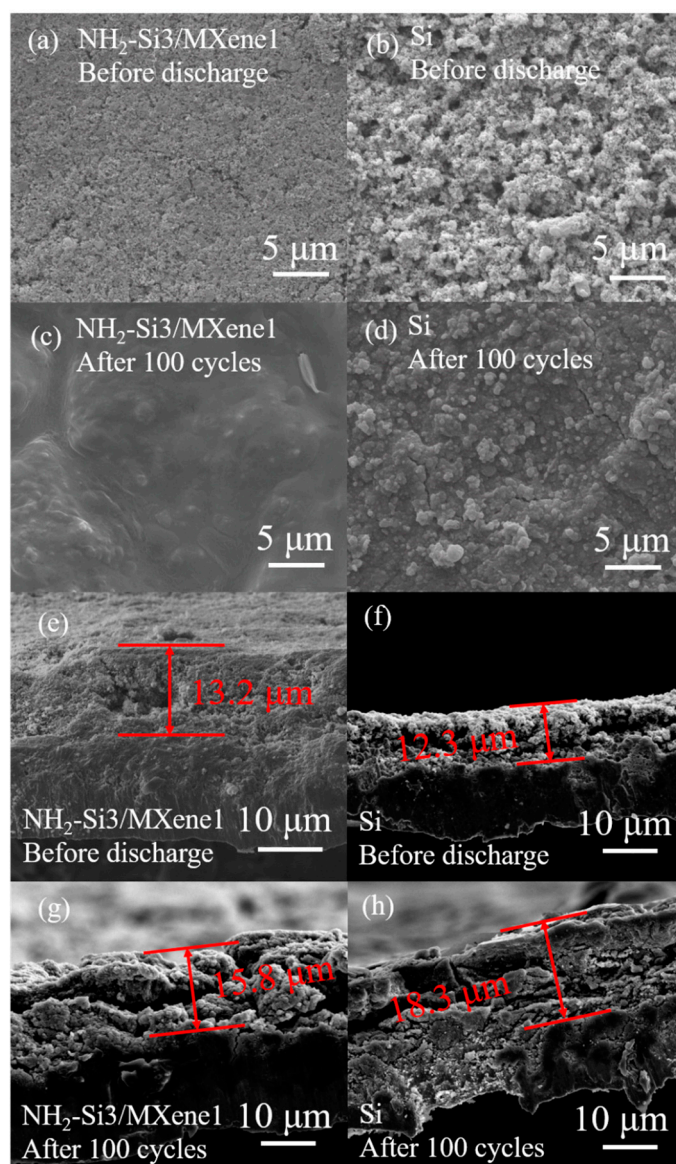


Figure 8. Top-view (a–d) and side-view (e–h) SEM images of $\text{NH}_2\text{-Si}_3/\text{MXene1}$ and Si electrodes before and after 100 cycles.

4. Conclusions

$\text{NH}_2\text{-Si}_3/\text{MXene1}$ composite with a stable porous structure was successfully synthesized and used as the negative electrode materials for LIBs. Positive-charged $\text{NH}_2\text{-Si}$ can be stably fixed on the surface of the negative-charged MXene nanosheets, which can protect Si from volume expansion issue and improve the electrical conductivity in the whole composite. At the same time, the interwoven MXene nanosheets provide an effective migration channel for lithium ions and constitute a stable conductive three-dimensional framework. Thus, the $\text{NH}_2\text{-Si}_3/\text{MXene1}$ negative electrode materials show good electrochemical performances. After 100 cycles, it could demonstrate a high specific discharge capacity of $1203.3 \text{ mAh g}^{-1}$ at a specific current of 0.2 A g^{-1} . The stable bonding mode and the strong porous structure can relieve the volume expansion problem of Si and put forward a new method for the development of lithium-ion negative electrode materials.

Supplementary Materials: The following supporting information can be downloaded at: <https://www.mdpi.com/article/10.3390/inorganics11070279/s1>, Figure S1: The XRD patterns of $\text{NH}_2\text{-Si}_1/\text{MXene}$ and $\text{NH}_2\text{-Si}_5/\text{MXene1}$; Figure S2: SEM images of (a,b) $\text{NH}_2\text{-Si}_1/\text{MXene1}$ and (c,d) $\text{NH}_2\text{-Si}_3/\text{MXene1}$.

Si5/MXene1; Figure S3: CVs of the first three cycles at 0.2 mV s^{-1} from 0.01 to 1.5 V for (a) $\text{NH}_2\text{-Si1/MXene1}$, (b) $\text{NH}_2\text{-Si5/MXene1}$, (c) MXene, and (d) Si.

Author Contributions: Experiments, H.Y.; data analysis H.Y.; writing—original draft preparation, H.Y.; writing—review and editing, H.Y., T.J. and Y.Z.; supervision, T.J. and Y.Z. All authors have read and agreed to the published version of the manuscript.

Funding: This work was supported by Natural Science Foundation of Hubei Province (2021CFB434).

Data Availability Statement: Not applicable.

Conflicts of Interest: The authors declare no conflict of interest.

References

1. Szczech, J.R.; Jin, S. Nanostructured silicon for high capacity lithium battery anodes. *Energy Environ. Sci.* **2011**, *4*, 56–72. [[CrossRef](#)]
2. Choi, J.; Wang, J.; Matsumoto, T. Si Swarf Wrapped by Graphite Sheets for Li-Ion Battery Electrodes with Improved Overvoltage and Cyclability. *J. Electrochem. Soc.* **2021**, *168*, 020521. [[CrossRef](#)]
3. Li, B.; Zhao, W.; Yang, Z.; Zhang, C.; Dang, F.; Liu, Y.; Jin, F.; Chen, X. A carbon-doped anatase TiO_2 -Based flexible silicon anode with high-performance and stability for flexible lithium-ion battery. *J. Power Sources* **2020**, *466*, 228339. [[CrossRef](#)]
4. Zhao, L.; He, Y.-B.; Li, C.; Jiang, K.; Wang, P.; Ma, J.; Xia, H.; Chen, F.; He, Y.; Chen, Z.; et al. Compact Si/C anodes fabricated by simultaneously regulating the size and oxidation degree of Si for Li-ion batteries. *J. Mater. Chem. A* **2019**, *7*, 24356–24365. [[CrossRef](#)]
5. Tian, X.; Xu, Q.; Cheng, L.; Meng, L.; Zhang, H.; Jia, X.; Bai, S.; Qin, Y. Enhancing the Performance of a Self-Standing Si/PCNF Anode by Optimizing the Porous Structure. *ACS Appl. Mater. Inter.* **2020**, *12*, 27219–27225. [[CrossRef](#)] [[PubMed](#)]
6. Yang, F.; Dai, Y.; Peng, D.; Huang, K. Synthesis of porous Si nanoparticles for high performances anode material in lithium-ion batteries. *Mater. Res. Express* **2021**, *8*, 025008. [[CrossRef](#)]
7. Xie, Q.; Qu, S.; Zhao, P. A facile fabrication of micro/nano-sized silicon/carbon composite with a honeycomb structure as high-stability anodes for lithium-ion batteries. *J. Electroanal. Chem.* **2021**, *884*, 115074. [[CrossRef](#)]
8. Hou, Y.-L.; Yang, Y.; Meng, W.-J.; Lei, B.-Y.; Ren, M.-X.; Yang, X.-X.; Wang, Y.-Q.; Zhao, D.-L. Core-shell structured Si@Cu nanoparticles encapsulated in carbon cages as high-performance lithium-ion battery anodes. *J. Alloys Compd.* **2021**, *874*, 159988. [[CrossRef](#)]
9. Song, C.; Zhao, B.; Chen, S.; Ma, J.; Du, H. Nickel-assisted one-pot preparation of graphenic carbon matrices embedded with silicon nanoparticles as anode materials for lithium ion batteries. *Carbon* **2021**, *179*, 266–274. [[CrossRef](#)]
10. Kwon, H.J.; Hwang, J.Y.; Shin, H.J.; Jeong, M.G.; Chung, K.Y.; Sun, Y.K.; Jung, H.G. Nano/Microstructured Silicon-Carbon Hybrid Composite Particles Fabricated with Corn Starch Biowaste as Anode Materials for Li-Ion Batteries. *Nano Lett.* **2020**, *20*, 625–635. [[CrossRef](#)]
11. Di, F.; Wang, N.; Li, L.; Geng, X.; Yang, H.; Zhou, W.; Sun, C.; An, B. Coral-like porous composite material of silicon and carbon synthesized by using diatomite as self-template and precursor with a good performance as anode of lithium-ions battery. *J. Alloys Compd.* **2021**, *854*, 157253. [[CrossRef](#)]
12. Xiang, B.; An, W.-L.; Fu, J.-J.; Mei, S.-X.; Guo, S.-G.; Zhang, X.-M.; Gao, B.; Chu, P.K. Graphene-encapsulated blackberry-like porous silicon nanospheres prepared by modest magnesiothermic reduction for high-performance lithium-ion battery anode. *Rare Met.* **2020**, *40*, 383–392. [[CrossRef](#)]
13. Yi, X.; Zhang, F.; Wang, J.; Wang, S.; Tong, H.; An, T.; Yu, W.-J. Facile synthesis of N-C/Si@G nanocomposite as a high-performance anode material for Li-ion batteries. *J. Alloys Compd.* **2021**, *872*, 159716. [[CrossRef](#)]
14. Phadatare, M.; Patil, R.; Blomquist, N.; Forsberg, S.; Ortegren, J.; Hummelgard, M.; Meshram, J.; Hernandez, G.; Brandell, D.; Leifer, K.; et al. Silicon-Nanographite Aerogel-Based Anodes for High Performance Lithium Ion Batteries. *Sci. Rep.* **2019**, *9*, 14621. [[CrossRef](#)]
15. Zeng, Y.; Huang, Y.; Liu, N.; Wang, X.; Zhang, Y.; Guo, Y.; Wu, H.-H.; Chen, H.; Tang, X.; Zhang, Q. N-doped porous carbon nanofibers sheathed pumpkin-like Si/C composites as free-standing anodes for lithium-ion batteries. *J. Energy Chem.* **2021**, *54*, 727–735. [[CrossRef](#)]
16. Ma, M.; Wang, H.; Li, X.; Peng, K.; Xiong, L.; Du, X. Free-standing SiOC/nitrogen-doped carbon fibers with highly capacitive Li storage. *J. Eur. Ceram. Soc.* **2020**, *40*, 5238–5246. [[CrossRef](#)]
17. Mei, S.; Liu, Y.; Fu, J.; Guo, S.; Deng, J.; Peng, X.; Zhang, X.; Gao, B.; Huo, K.; Chu, P.K. Waste-glass-derived silicon/CNTs composite with strong Si-C covalent bonding for advanced anode materials in lithium-ion batteries. *Appl. Surf. Sci.* **2021**, *563*, 150280. [[CrossRef](#)]
18. Wang, Y.-Q.; Yang, X.-X.; Ren, M.-X.; Lei, B.-Y.; Hou, Y.-L.; Meng, W.-J.; Zhao, D.-L. 3D CNTs networks enable core-shell structured Si@Ni nanoparticle anodes with enhanced reversible capacity and cyclic performance for lithium ion batteries. *Int. J. Hydrogen Energy* **2021**, *46*, 16179–16187. [[CrossRef](#)]
19. Zhang, X.; Hayashida, R.; Tanaka, M.; Watanabe, T. Synthesis of carbon-coated silicon nanoparticles by induction thermal plasma for lithium ion battery. *Powder Technol.* **2020**, *371*, 26–36. [[CrossRef](#)]

20. Wen, Y.; Rufford, T.E.; Chen, X.; Li, N.; Lyu, M.; Dai, L.; Wang, L. Nitrogen-doped $\text{Ti}_3\text{C}_2\text{T}_x$ MXene electrodes for high-performance supercapacitors. *Nano Energy* **2017**, *38*, 368–376. [[CrossRef](#)]
21. Xie, Y.; Gao, F.; Tu, X.; Ma, X.; Xu, Q.; Dai, R.; Huang, X.; Yu, Y.; Lu, L. Facile Synthesis of MXene/Electrochemically Reduced Graphene Oxide Composites and Their Application for Electrochemical Sensing of Carbendazim. *J. Electrochem. Soc.* **2019**, *166*, B1673–B1680. [[CrossRef](#)]
22. Naguib, M.; Come, J.; Dyatkin, B.; Presser, V.; Taberna, P.-L.; Simon, P.; Barsoum, M.W.; Gogotsi, Y. MXene: A promising transition metal carbide anode for lithium-ion batteries. *Electrochem. Commun.* **2012**, *16*, 61–64. [[CrossRef](#)]
23. Li, X.; Chen, Z.; Li, A.; Yu, Y.; Chen, X.; Song, H. Three-Dimensional Hierarchical Porous Structures Constructed by Two-Stage MXene-Wrapped Si Nanoparticles for Li-Ion Batteries. *ACS Appl. Mater. Inter.* **2020**, *12*, 48718–48728. [[CrossRef](#)] [[PubMed](#)]
24. Xia, M.; Chen, B.; Gu, F.; Zu, L.; Xu, M.; Feng, Y.; Wang, Z.; Zhang, H.; Zhang, C.; Yang, J. $\text{Ti}_3\text{C}_2\text{T}_x$ MXene Nanosheets as a Robust and Conductive Tight on Si Anodes Significantly Enhance Electrochemical Lithium Storage Performance. *ACS Nano* **2020**, *14*, 5111–5120. [[CrossRef](#)]
25. Jiang, M.; Jiang, M.; Gao, H.; Chen, J.; Liu, W.; Ma, Y.; Luo, W.; Yang, J. Comparison of Additives in Anode: The Case of Graphene, MXene, CNTs Integration with Silicon Inside Carbon Nanofibers. *Acta Metall. Sin Engl.* **2020**, *34*, 337–346. [[CrossRef](#)]
26. Zhang, F.; Jia, Z.; Wang, C.; Feng, A.; Wang, K.; Hou, T.; Liu, J.; Zhang, Y.; Wu, G. Sandwich-like silicon/ $\text{Ti}_3\text{C}_2\text{T}_x$ MXene composite by electrostatic self-assembly for high performance lithium ion battery. *Energy* **2020**, *195*, 117047. [[CrossRef](#)]
27. Yang, Q.; Wang, Z.; Xia, Y.; Wu, G.; Chen, C.; Wang, J.; Rao, P.; Dong, A. Facile electrostatic assembly of Si@MXene superstructures for enhanced lithium-ion storage. *J. Colloid Interface Sci.* **2020**, *580*, 68–76. [[CrossRef](#)]
28. Gou, L.; Jing, W.; Li, Y.; Wang, M.; Hu, S.; Wang, H.; He, Y.-B. Lattice-Coupled Si/MXene Confined by Hard Carbon for Fast Sodium-Ion Conduction. *ACS Appl. Energy Mater.* **2021**, *4*, 7268–7277. [[CrossRef](#)]
29. Zhang, X.; Zhang, Z.; Zhou, Z. MXene-based materials for electrochemical energy storage. *J. Energy Chem.* **2018**, *27*, 73–85. [[CrossRef](#)]
30. Xiong, D.; Li, X.; Bai, Z.; Lu, S. Recent Advances in Layered $\text{Ti}_3\text{C}_2\text{T}_x$ MXene for Electrochemical Energy Storage. *Small* **2018**, *14*, 1703419. [[CrossRef](#)]
31. Li, X.; Bai, Y.; Wang, M.; Wang, G.; Ma, Y.; Li, L.; Xiao, B.; Zheng, J. Self-assembly encapsulation of Si in N-doped reduced graphene oxide for use as a lithium ion battery anode with significantly enhanced electrochemical performance. *Sustain. Energy Fuels* **2019**, *3*, 1427–1438. [[CrossRef](#)]
32. Kong, F.; He, X.; Liu, Q.; Qi, X.; Sun, D.; Zheng, Y.; Wang, R.; Bai, Y. Enhanced reversible Li-ion storage in Si@ Ti_3C_2 MXene nanocomposite. *Electrochem. Commun.* **2018**, *97*, 16–21. [[CrossRef](#)]
33. Xiao, W.; Qiu, Y.; Xu, Q.; Wang, J.; Xie, C.; Peng, J.; Hu, J.; Zhang, J.; Li, X. Building sandwich-like carbon coated Si@CNTs composites as high-performance anode materials for lithium-ion batteries. *Electrochim. Acta* **2020**, *364*, 137278. [[CrossRef](#)]
34. Xiang, J.; Liu, H.; Na, R.; Wang, D.; Shan, Z.; Tian, J. Facile preparation of void-buffered Si@ TiO_2 /C microspheres for high-capacity lithium ion battery anodes. *Electrochim. Acta* **2020**, *337*, 135841. [[CrossRef](#)]
35. Zheng, M.; Wu, S. A novel method for synthesizing $\text{Ti}_3\text{C}_2\text{T}_x$ MXene nanosheets supported Si nanoparticles as lithium-ion batteries anode for electric vehicles applications. *Mater. Lett.* **2022**, *311*, 131570. [[CrossRef](#)]
36. Muráth, S.; Varga, T.; Kukovecz, Á.; Kónya, Z.; Sipos, P.; Pálkó, I.; Varga, G. Morphological aspects determine the catalytic activity of porous hydrocalumites: The role of the sacrificial templates. *Mater. Today Chem.* **2022**, *23*, 100682. [[CrossRef](#)]
37. Tian, Y.; An, Y.; Feng, J. Flexible and Freestanding Silicon/MXene Composite Papers for High-Performance Lithium-Ion Batteries. *ACS Appl. Mater. Inter.* **2019**, *11*, 10004–10011. [[CrossRef](#)]
38. Wang, T.; Ji, X.; Wu, F.; Yang, W.; Dai, X.; Xu, X.; Wang, J.; Guo, D.; Chen, M. Facile fabrication of a three-dimensional coral-like silicon nanostructure coated with a C/rGO double layer by using the magnesiothermic reduction of silica nanotubes for high-performance lithium-ion battery anodes. *J. Alloys Compd.* **2021**, *863*, 158569. [[CrossRef](#)]
39. Zhang, Y.; Mu, Z.; Lai, J.; Chao, Y.; Yang, Y.; Zhou, P.; Li, Y.; Yang, W.; Xia, Z.; Guo, S. MXene/Si@ SiO_x @C Layer-by-Layer Superstructure with Autoadjustable Function for Superior Stable Lithium Storage. *ACS Nano* **2019**, *13*, 2167–2175. [[CrossRef](#)]
40. Wang, C.; Yang, Y.; Lu, D.; Guan, R.; Wang, J.; Bian, X. Si-based composite deriving from wok ash waste as high-performance anode for Li-ion battery. *J. Alloys Compd.* **2021**, *858*, 157680. [[CrossRef](#)]
41. Yu, J.; Zhang, C.; Wu, W.; Cai, Y.; Zhang, Y. Nodes-connected silicon-carbon nanofibrous hybrids anodes for lithium-ion batteries. *Appl. Surf. Sci.* **2021**, *548*, 148944. [[CrossRef](#)]
42. Chandrasekaran, R.; Fuller, T.F. Analysis of the Lithium-Ion Insertion Silicon Composite Electrode/Separator/Lithium Foil Cell. *J. Electrochem. Soc.* **2011**, *158*, A859–A871. [[CrossRef](#)]
43. Cheng, R.; Hu, T.; Zhang, H.; Wang, C.; Hu, M.; Yang, J.; Cui, C.; Guang, T.; Li, C.; Shi, C.; et al. Understanding the Lithium Storage Mechanism of $\text{Ti}_3\text{C}_2\text{T}_x$ MXene. *J. Phys. Chem. C* **2018**, *123*, 1099–1109. [[CrossRef](#)]
44. Li, H.; Lu, M.; Han, W.; Li, H.; Wu, Y.; Zhang, W.; Wang, J.; Zhang, B. Employing MXene as a matrix for loading amorphous Si generated upon lithiation towards enhanced lithium-ion storage. *J. Energy Chem.* **2019**, *38*, 50–54. [[CrossRef](#)]
45. Wei, C.; Fei, H.; Tian, Y.; An, Y.; Tao, Y.; Li, Y.; Feng, J. Scalable construction of SiO/wrinkled MXene composite by a simple electrostatic self-assembly strategy as anode for high-energy lithium-ion batteries. *Chin. Chem. Lett.* **2020**, *31*, 980–983. [[CrossRef](#)]
46. Zhou, H.; Cui, C.; Cheng, R.; Yang, J.; Wang, X. MXene Enables Stable Solid-Electrolyte Interphase for Si@MXene Composite with Enhanced Cycling Stability. *ChemElectroChem* **2021**, *8*, 3089–3094. [[CrossRef](#)]

47. Wang, Z.; Cao, D.; Ren, M.; Zhang, H.; Pan, L.; John Zhang, C.; Yang, J. Si@Ti₃C₂T_x with Si nanoparticles embedded in a 3D conductive network of crumpled Ti₃C₂T_x nanosheets for the anode of lithium-ion batteries with enhanced cycling performance. *J. Alloys Compd.* **2022**, *892*, 162037. [[CrossRef](#)]
48. Wang, Z.; Xu, Z.; Huang, H.; Chu, X.; Xie, Y.; Xiong, D.; Yan, C.; Zhao, H.; Zhang, H.; Yang, W. Unraveling and Regulating Self-Discharge Behavior of Ti₃C₂T_x MXene-Based Supercapacitors. *ACS Nano* **2020**, *14*, 4916–4924. [[CrossRef](#)]
49. Zhang, K.; Zhao, D.; Qian, Z.; Gu, X.; Yang, J.; Qian, Y. N-doped Ti₃C₂T_x MXene sheet-coated SiO_x to boost lithium storage for lithium-ion batteries. *Sci. China Mater.* **2022**, *66*, 51–60. [[CrossRef](#)]
50. Zhang, Z.; Ying, H.; Huang, P.; Zhang, S.; Zhang, Z.; Yang, T.; Han, W.-Q. Porous Si decorated on MXene as free-standing anodes for lithium-ion batteries with enhanced diffusion properties and mechanical stability. *Chem. Eng. J.* **2023**, *451*, 138785. [[CrossRef](#)]
51. Shao, T.; Liu, J.; Gan, L.; Gong, Z.; Long, M. Yolk-shell Si@void@C composite with Chito-oligosaccharide as a C–N precursor for high capacity anode in lithium-ion batteries. *J. Phys. Chem. Solids* **2021**, *152*, 109965. [[CrossRef](#)]

Disclaimer/Publisher’s Note: The statements, opinions and data contained in all publications are solely those of the individual author(s) and contributor(s) and not of MDPI and/or the editor(s). MDPI and/or the editor(s) disclaim responsibility for any injury to people or property resulting from any ideas, methods, instructions or products referred to in the content.